DLSR: A solution to the parallax artefact in X-ray diffraction computed tomography data

Vamvakeros A.[a,b]*, Coelho A. A.[c], Matras D.[a,d,e], Dong H.[b], Odarchenko Y.[a], Price S.W.T.[a], Butler K.T.[f], Gutowski O.[g], Dippel A.C.[g], v. Zimmerman M.[g], Martens I.[h], Drnec J.[h], Beale A.M.[a,b,i]*, Jacques S.D.M.[a]*

a) Finden Limited, Merchant House, 5 East St Helens Street, Abingdon, OX14 5EG, United Kingdom

b) Department of Chemistry, University College London, 20 Gordon Street, London WC1H 0AJ, United Kingdom

c) Coelho Software, 72 Cedar Street, Wynnum, Brisbane, Queensland 4178, Australia

d) Current affiliation: Diamond Light Source, Harwell Science and Innovation Campus, Didcot, Oxfordshire OX11 0DE, United Kingdom

e) Current affiliation: The Faraday Institution, Quad One, Harwell Science and Innovation Campus, Didcot, OX11 0RA, United Kingdom

f) SciML, Scientific Computer Division, Rutherford Appleton Laboratory, Harwell OX11 0QX, United Kingdom

g) Deutsches Elektronen-Synchrotron DESY, Notkestraße 85, 22607 Hamburg, Germany

h) ESRF - The European Synchrotron, Grenoble 38000, France

i) Research Complex at Harwell, Rutherford Appleton Laboratory, Harwell Science and Innovation Campus, Didcot, Oxon OX11 0FA, United Kingdom

*correspondence email: antony@finden.co.uk, andrew.beale@ucl.ac.uk, simon@finden.co.uk

Abstract

A new tomographic reconstruction algorithm is presented, termed Direct Least-Squares Reconstruction (DLSR), which solves the well-known parallax problem in X-ray scattering-based experiments. The parallax artefact arises from relatively large samples where X-rays, scattered from a scattering angle 2θ, arrive at multiple detector elements. This phenomenon leads to loss of physico-chemical information associated with diffraction peak shape and position (i.e. altering the calculated crystallite size and lattice parameter values respectively) and is currently the major barrier to investigating samples and devices at the cm-level (scale-up problem). The accuracy of the DLSR algorithm has been tested against simulated and experimental X-ray diffraction computed tomography data using the TOPAS software.

Synopsis

A new reconstruction approach is presented that can directly yield physico-chemical images and overcome the parallax problem in X-ray diffraction computed tomography (XRD-CT) experiments.

Keywords

Scattering; Tomography; XRD; WAXS; PDF

Introduction

X-ray diffraction computed tomography (XRD-CT) is a pencil beam scanning tomographic technique yielding reconstructed images corresponding to a sample's cross section (Harding *et al.*, 1987). The contrast in these images arises from differences in the signal of the scattered/diffracted X-rays. In conventional X-ray absorption-contrast computed tomography (X-ray CT), contrast arises from differences in the density of the sample. For this reason, XRD-CT is able to spatially-resolve chemical species of similar density where conventional X-ray CT often fails. This property of XRD-CT explains why this technique is sometimes referred to as Diffraction/Scattering Computed Tomography (DSCT). This clarification avoids confusion to newcomers in the field. The first synchrotron implementation of the technique was performed in 1998 by Kleuker *et al.* (Kleuker *et al.*, 1998) at the medical imaging beamline of the ESRF. However, it was the work of Stock *et al.* (Stock *et al.*, 2008) in 2007 and Bleuet *et al.* (Bleuet *et al.*, 2008) in 2008, at the APS and ESRF synchrotrons respectively, that re-introduced the technique to a wider audience.

Since then, the potential of XRD-CT as a characterisation tool has been realised; it has been applied to a wide range of materials systems including cultural heritage paints (Vanmeert *et al.*, 2015; Price *et al.*, 2019; Gonzalez *et al.*, 2020), automotive paints (De Nolf & Janssens, 2010), ceramic cement (Artioli *et al.*, 2010; Valentini *et al.*, 2011, 2012; Voltolini *et al.*, 2013; Claret *et al.*, 2018), uranium-based materials for nuclear reactor applications (Palancher *et al.*, 2011; Bonnin *et al.*, 2014), high pressure disordered graphite (Álvarez-Murga *et al.*, 2011), Al-matrix SiC-monofilament composites (Stock & Almer, 2012), solid catalysts (Basile *et al.*, 2010; Ruiz-Martínez *et al.*, 2013; Beale, Gibson *et al.*, 2014; Price, Ignatyev *et al.*, 2015; Wragg *et al.*, 2015; Ihli *et al.*, 2017; Grande *et al.*, 2020; Gambino *et al.*, 2020), batteries and battery electrodes (Jensen *et al.*, 2015; Daemi *et al.*, 2020), fuel cells (Sanchez *et al.*, 2017; Heenan *et al.*, 2020) and biological samples/ samples used for biological applications (Egan *et al.*, 2013; Leemreize *et al.*, 2013; Cedola *et al.*, 2013; Gürsoy *et al.*, 2015; Frølich & Birkedal, 2015; Wittig *et al.*, 2019). Importantly, apart from the aforementioned static scans at ambient conditions, XRD-CT has been applied to study heterogeneous catalysts during preparation (Jacques *et al.*, 2011), activation (Jacques *et al.*, 2013; Senecal *et al.*, 2017) and indeed under reaction conditions (O'Brien *et al.*, 2012; Price, Geraki *et al.*, 2015; Vamvakeros, Jacques, Middelkoop *et al.*, 2015; Sheppard *et al.*, 2017; Price *et al.*, 2017; Beale *et al.*, 2018; Matras *et al.*, 2018; Vamvakeros *et al.*, 2018; Middelkoop *et al.*, 2019; Matras *et al.*, 2019; Matras, Vamvakeros, Jacques, Grosjean *et al.*, 2020; Matras, Vamvakeros, Jacques, Middelkoop *et al.*, 2020; Vamvakeros, Matras, Jacques, di Michiel, Price *et al.*, 2020; Vamvakeros, Matras, Jacques, di Michiel, Middelkoop *et al.*, 2020). It has also been successfully applied to other operating functional materials and devices, such as electrodes used in Li-ion (Finegan *et al.*, 2019; Liu *et al.*, 2019; Finegan *et al.*, 2020), Li-S (Tonin *et al.*, 2020) and Na-ion (Sottmann *et al.*, 2017) batteries as well as in proton exchange membrane (PEM) (Martens *et al.*, 2019, 2020) and solid oxide fuel cells (SOFCs) (Li *et al.*, 2019).

In synchrotron XRD-CT, the sample is probed using a narrow focused monochromatic X-ray beam also known as a "pencil-beam". There exist several different acquisition strategies, such as the bisection/interlaced (Anders P. Kaestner *et al.*, 2011; Vamvakeros *et al.*, 2016) and the continuous rotation-translation (Vamvakeros *et al.*, 2018) methods, the simplest being a zigzag approach comprising a series of linescans each performed at a different tomographic angle. A 2D diffraction pattern is collected at each translation step (nT steps) at each tomographic angle (nA angles) in transmission geometry using an area detector. After the azimuthal integration of the 2D diffraction patterns, the data are reshaped to form a stack of sinograms with nT × nA × nB dimensions, where nB are the chosen number of bins for the 1d diffraction patterns.

Reconstruction algorithms

Conventional

The data analysis performed in most studies is termed “reverse-analysis” (Bleuet *et al.*, 2008) where each sinogram is independently reconstructed using conventional tomographic reconstruction algorithms. The process yields an image where each voxel corresponds to a local diffraction pattern (or a stack of nB images, with nT × nT dimensions, each corresponding to one bin in the 1d diffraction patterns). The analysis of these spatially-resolved diffraction patterns can vary from simple single peak sequential batch fitting to a one step full profile analysis, termed “Rietveld-CT” (Wragg *et al.*, 2015). The latter approach is superior to the commonly used sequential approach as global parameters are shared between all local models (e.g. zero error, instrumental broadening); this stabilises the refinements. To clarify, each voxel in the reconstructed images consists of a local model (e.g. multi-phase scale factors, lattice parameters and crystallite sizes) refined against the respective local diffraction pattern. This means that only the global parameters are shared amongst the local models. Rietveld-CT has only been demonstrated on small images (i.e. 60 × 60 voxels); with larger images dependent on available computer memory). Regardless of the data analysis strategy, the final results are nP images containing local physico-chemical information (Figure 1), where nP is the number of refined parameters in the local models (e.g. maps corresponding to scale factors, lattice parameters and crystallite sizes). It should be noted that in all the aforementioned approaches, fitting is performed using the reconstructed diffraction patterns which are of inferior quality to the projected diffraction patterns present in the sinograms.

Direct Least-Squares Reconstruction

In contrast, the “Direct Least-Squares Reconstruction” (DLSR) algorithm combines the reconstruction and fitting steps into a single step, yielding nP physico-chemical images with nT × nT size (or a matrix with nT × nT × nP dimensions) directly from the sinograms (nT × nA × nB). To achieve this, an empty canvas is first created equal to the size of the translation steps in the sinograms (nT × nT). Each pixel is then associated with a local model and the reconstruction process is performed by solving the $A x = b$ system of equations. Local models that are linear can be solved with iterative reconstruction algorithms commonly used in computed tomography (Beister *et al.*, 2012). These techniques can be used in the DLSR algorithm for certain chemical tomography techniques, where the analysis involves a linear combination of scattering pattern or spectra, such as the linear combination fitting approach used in X-ray absorption near edge structure CT (XANES-CT). In XRD-CT, the local models comprise a large nonlinear set of equations which are solved using DLSR. Although DLSR is clearly a computationally expensive reconstruction algorithm, it has the benefit of being inherently stable as many parameters are shared. The DLSR algorithm tries to solve a modified A x = b system of nonlinear equations using a nonlinear least-squares minimization approach, where:

- *A* is a (nT × nA × nB, nT × nT × nB) dimension sparse coefficient matrix corresponding to ray tracing during the tomographic scan
- *x* is a (nT × nT × nB, 1) dimension matrix containing the nT × nT nonlinear models.
- *b* is a (nT × nA × nB, 1) dimension matrix which corresponds to the stack of sinograms.

When the nT × nT models use an P degree polynomial (instead of the non-linear used to model peak shapes in diffraction patterns) to fit the nT × nA × nB intensities, then the system becomes linear. For P = 0 and nB = 1, the system reverts to the system of linear equations A x = b used in conventional tomography to reconstruct one image (nT × nT) from one sinogram (nT × nA) with A having (nT × nA, nT × nT) dimensions.

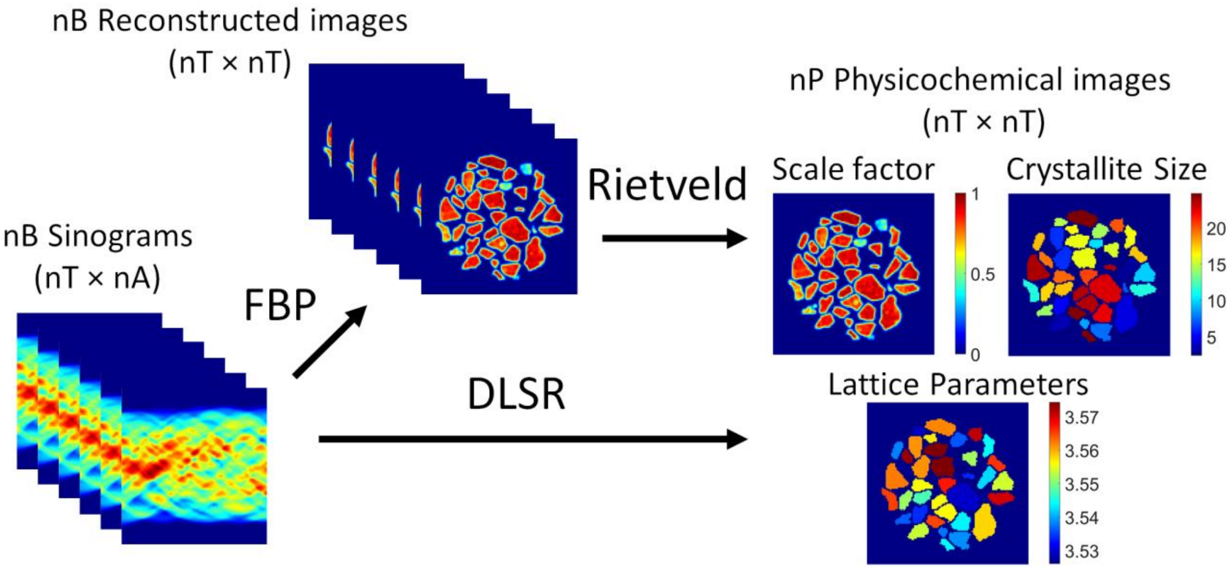

Figure 1: Schematic representation of the conventional data analysis route used in XRD-CT (top-row) and the DLSR approach (bottom row) which yields physico-chemical images in a single step.

In order to reconstruct the XRD-CT data, we implemented the DLSR algorithm in the well-known TOPAS software; it was chosen because of its speed (written in C++), robustness and ability to handle large amounts of diffraction data (Coelho, 2018).

Parallax Artefact

The DLSR/TOPAS approach overcomes the well-known parallax artefact but it can also be applied to artefact-free XRD-CT data. Specifically, in scattering-based CT experiments, it is assumed the scattered/diffracted X-rays at any given scattering angle 2θ along the sample thickness arrive at the same detector element; this is illustrated in panel a of Figure 2. This assumption is valid when the sample thickness is relatively thin (typically in the order of a few mm). In thick samples, the assumption is not valid as diffracted X-rays at a particular 2θ angle arrive at a multitude of detector elements; this is due to varying distances between sample elements and the detector. The phenomenon is known as the parallax effect and has a *tan(2θ)* dependence (Harding *et al.*, 1987; Beale, Jacques *et al.*, 2014). The parallax effect is illustrated in Figure 2b. The artefact takes the form of a peak shift and peak broadening and even peak splitting (Scarlett *et al.*, 2011).

Recently Stock et al. suggested a simple approach to overcome the parallax artefact (Stock *et al.*, 2019):

1. A translation scan is performed at a tomographic angle phi
2. The same translation scan is performed at a tomographic angle 180 ° + phi
3. Full profile analysis of the acquired diffraction patterns in order to extract the lattice parameter values for the various structure models
4. The mean value of the lattice parameter values for each position is calculated using the diffraction patterns from the two angles

Unfortunately, this approach is only applicable to fairly homogeneous samples where a single unit cell is used to accurately model the acquired diffraction pattern per translation step. This problem will be illustrated in a later section using experimental data where it is shown that the 0-360° approach does not solve the parallax problem. We have previously pointed out that it can be dangerous to use a single structure model to fit diffraction patterns collected from heterogeneous samples (Vamvakeros *et al.*, 2016). As an example, if a phase is present as small crystallites (generating broad peaks) in some sample regions and larger crystallites elsewhere (generating sharp diffraction peaks), then using a single structure model can lead to wrong values for both peak positions (lattice parameters) and peak shapes/FWHM (crystallite sizes). If the diffraction patterns are collected using a tomographic approach, then the local information can be retrieved using the “reverse analysis” approach or the DLSR approach. In the latter, nM structure models are used to fit the acquired diffraction patterns (where nM is derived from ray tracing) overcoming the aforementioned problem.

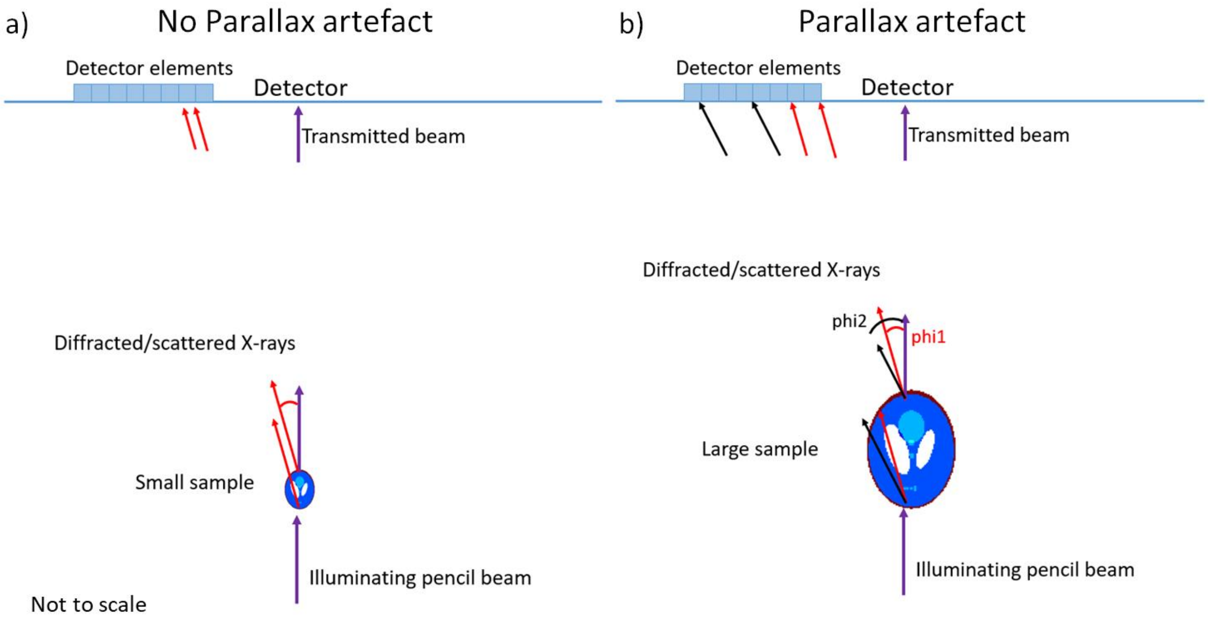

Figure 2: a) Schematic representation of an XRD pattern collected in transmission geometry with an area detector when there is no parallax artefact. The scattered X-rays at a given 2θ angle along the sample arrive at the same detector element. b) Illustration of a diffraction measurement in transmission geometry with parallax artefact. The X-rays scattered/diffracted along the sample at a certain 2θ angle arrive at different detector elements leading to peak broadening and even peak splitting.

To clarify, in this work we are looking at the parallax artefact from the sample's view point and it should not be confused with detector parallax artefact. The latter is associated with X-ray photons traversing multiple detector pixels at high *2θ* angles for detectors with thick sensors. Detector parallax also results in peak position and peak shape artefacts; the former can be corrected using a simple quadratic polynomial as demonstrated by Marlton et al. (Marlton *et al.*, 2019).

In this work, we show that the DLSR approach accurately reconstructs physico-chemical images from XRD-CT data containing parallax artefact. First, we demonstrate the DLSR approach using simulated artefact-free XRD-CT data and simulated XRD-CT data containing parallax artefact. Then we apply it to experimental XRD-CT data collected from a large phantom sample designed specifically for a parallax XRD-CT measurement.

Methods & Materials

The powder samples measured in this work were SiC (nanopowder, <100 nm particle size, 594911-100G, Sigma-Aldrich), TiO_2 Rutile (204757-25G, Sigma-Aldrich) and MgO (307742-500G, Sigma-Aldrich). The three powder samples were mounted into separate glass pipettes with an outer diameter of ca. 7.5 mm supported by quartz wool from both ends. Two pipettes were prepared using the same MgO powder sample. The four glass pipettes containing the powder samples were mounted onto a 3D printed sample holder designed for the parallax experiment. Photographs of the experimental setup are provided in Figure S1.

XRD-CT measurements were performed at beamline station P07 (EH2) at PETRA III, DESY, using a 103.5 keV (λ = 0.11979 Å) monochromatic X-ray beam focused to a spot size of 20 × 3 μm (H × V). 2D powder diffraction patterns were collected using a Pilatus3 X CdTe 2 M hybrid photon counting area detector. The 3D printed sample holder was mounted directly on the rotation stage. The rotation stage was mounted perpendicularly to a hexapod; the hexapod was used to translate the sample across the beam. The XRD-CT scans were measured by performing a series of zigzag line scans in the z (vertical) direction using the hexapod and rotation steps. Two XRD-CT scans were performed, in both cases the number of translation steps were 300 with a 80 μm step size and a 10 ms exposure time per point. The first XRD-CT scan was performed over a 0-180° range while the second over a 0-360° range, both using 300 angular steps. The detector calibration was performed using a CeO_2 standard. Every 2D diffraction image was calibrated and azimuthally integrated to a 1D powder diffraction pattern with a 10 % trimmed mean filter using the pyFAI software package and in-house developed scripts (Vamvakeros, Jacques, Di Michiel *et al.*, 2015). The integrated diffraction patterns were reshaped into sinograms and centered; the air scatter signal was subtracted from the data. Due to computational constraints, the data were rebinned to form a stack of sinograms with a size of 121 × 121 voxels. For the conventional data analysis approach, the final XRD-CT images (i.e. reconstructed data volume) were reconstructed using the filtered back projection algorithm.

Rietveld analysis was performed on the reconstructed diffraction patterns with the TOPAS software on a voxel by voxel basis. The results from the refinements were imported into MATLAB in order to create the various figures presented (i.e. phase distribution maps based on the scale factors, lattice parameters and crystallite sizes). Rietveld analysis was first performed using the summed diffraction pattern of each XRD-CT dataset (i.e. to provide a good starting model) before running the voxel-by-voxel Rietveld analysis to provide the spatially-resolved physico-chemical information. A 3XS Data Science Workstation C264X2 with 2x Intel Xeon Silver 4216 and 512 GB RAM was used to perform the refinements.

Results & Discussion

Simulated XRD-CT data without parallax

The TOPAS implementation of the DLSR algorithm was first tested using simulated XRD-CT data. Instead of using synthetic images such as the Shepp-Logan phantom, a far more realistic and challenging image was used for the simulation tests. This image was derived from the Rietveld analysis of previously collected XRD-CT from a Mn-Na-W/SiO2 catalyst, specifically the scale factor map of the cristobalite phase which is the catalyst support material which accurately describes the catalyst particles (Vamvakeros, Matras, Jacques, di Michiel, Price *et al.*, 2020). For simplicity, a cubic Ni fcc structure (ICSD: 64989 (1953)) was used in the proof-of-concept DLSR simulation tests. However, as it will be shown in the experimental data section, there is no symmetry or single-phase limitation to the DLSR approach as it can be used for multiphase systems.

First, image segmentation was performed using the intensity image to isolate the 36 catalyst particles. Each particle was then labelled and a single diffraction pattern assigned. Specifically, 36 Ni diffraction patterns were simulated using TOPAS by assigning a random value for lattice parameter and crystallite size (i.e. in the range of 3.525 - 3.575 Å and 2 - 25 nm respectively) using the fundamental parameters (*FP)* peak shape and the same X-ray energy and Q range as in the experimental XRD-CT data presented at a later section in this work. The segmented (binary) image was used to create a 3D volume by assigning a Ni diffraction pattern to all pixels describing the corresponding particle. This 3D volume was then multiplied by the intensity map leading to the simulated Ni XRD-CT dataset. This XRD-CT dataset was then forward projected using the *AIR tools II* (Hansen & Jørgensen, 2018) in MATLAB to create the stack of sinograms using 121 angles covering a 0-180° angular range (121 × 121 × 2048). These sinograms were used for the simulation tests.

The results obtained from the Rietveld analysis of the simulated Ni XRD-CT data using the conventional and DLSR approaches are presented in Figure 3. For the conventional approach, each sinogram was reconstructed using the filtered back projection (FBP) algorithm and then sequential full profile analysis was performed using TOPAS guided by in-house developed MATLAB scripts. For the TOPAS implementation of the DLSR approach, a single input file was created containing all XRD patterns present in the sinograms (121 × 121 *xdds* in TOPAS) and assigning nT × nT (121 × 121) Ni structure models per pattern (i.e. per *xdd*). The nT × nT structure models correspond to the number of pixels (size) of the reconstructed XRD-CT images. Each Ni structure associated with each (projection) pattern was multiplied by a scalar which was calculated by the ray tracing using the *AIR tools II* package (*A* matrix). To clarify, these nT × nT structure models were constrained to be the same for each of the nT × nA diffraction patterns present in the sinogram volume (the same nT x nT structures are used in every nT x nA xdd using *peak_buffer_similar_tag accordingly* to speed up the code). The Ni parameters refined were the scale factor, lattice parameter and crystallite size. This input file was then executed by TOPAS which solved the nT × nA (121 × 121) system of nonlinear equations. Unfortunately, as expected, this approach is computationally expensive and requires many 10s to 100s of GBs of RAM depending on image size and number of diffraction patterns (see also section S3). However, these requirements can be significantly decreased by masking the non-sample voxels (i.e. void) without a decrease in quality of the reconstructed images (see sections S3-4). For this reason, this approach was used for all DLSR results presented in this work. The impact of the number of projections and number of peaks in the diffraction patterns were also investigated (sections S5-6). For the simulated Ni XRD-CT data, a single diffraction peak was used to reconstruct the images (additional reflections are unnecessary due to the high symmetry cubic unit cell).

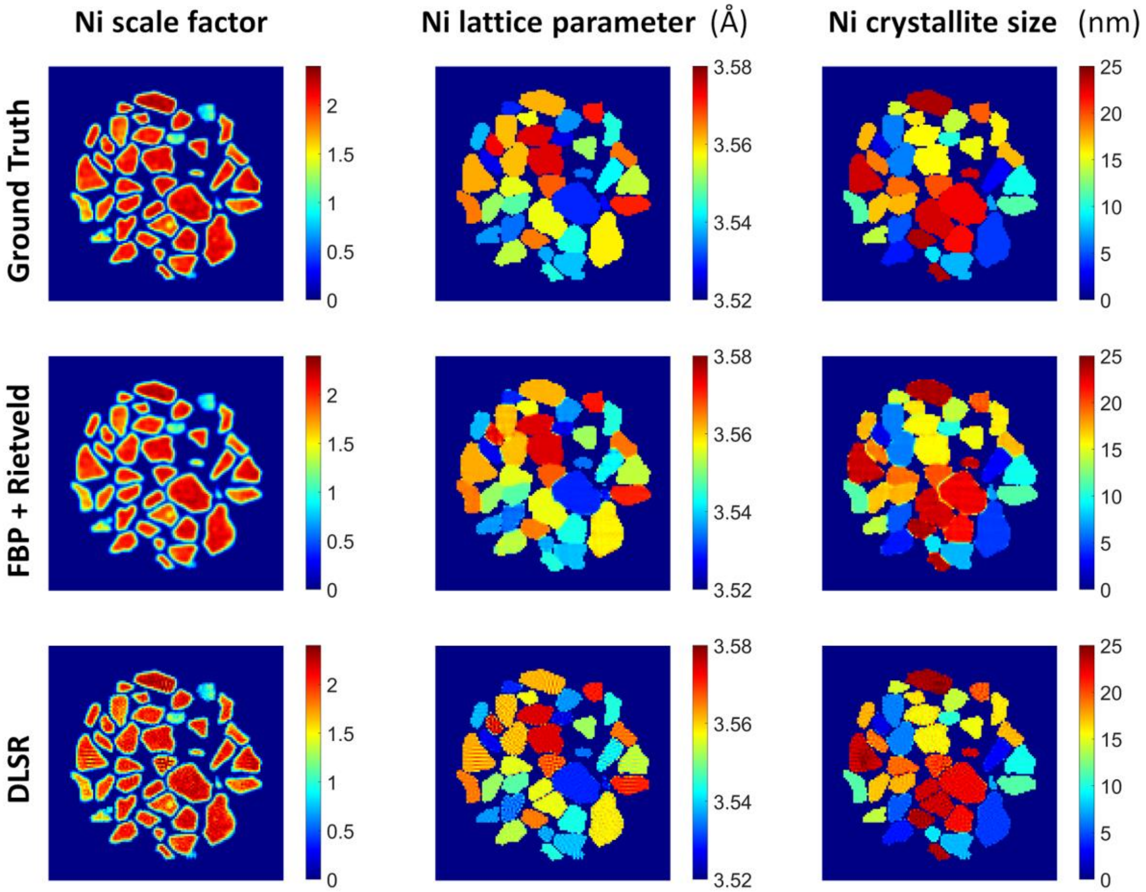

Figure 3: Parallax-free XRD-CT simulations. Top row: The ground truth images from the simulated Ni XRD-CT data, Middle row: Results obtained from the sequential Rietveld analysis of the reconstructed XRD-CT data, Bottom row: Images derived from the Rietveld reconstruction of the XRD-CT data using the DLSR approach.

As shown in Figure 3, the DLSR approach is able to reconstruct correctly the Ni phase distribution map (i.e. absolute values for the Ni scale factor), the Ni lattice parameter and Ni crystallite size maps. However, it should be noted that there is no real advantage with DLSR over the conventional approach in the absence of parallax artefact. As shown in section S3, the DLSR approach is computationally expensive and requires significantly more time than the conventional approach. Nevertheless, the results presented in Figure 3 serve as a proof of concept; the method works and converges to the correct values for the various parameters (DLSR Rwp = 0.59 % after 23 iterations in 13.1 min using 25 GB of RAM).

Simulated XRD-CT data with parallax

The DLSR approach however was designed to treat XRD-CT data containing parallax artefact and to reconstruct parallax artefact-free physicochemical images. To achieve this, we first simulated XRD-CT sinogram data containing parallax artefact. This is important as having a parallax forward projector allows for a wide range of minimisation techniques and not just limited to least squares. Assuming that the sample is at tomographic angle 0° and illuminated with a pencil beam, then assuming nT voxels along the sample thickness allows us to model the parallax phenomenon by assigning nT 2θ axes (i.e. a vector containing nT 2θ axis). The 2θ axis assigned at each voxel is related to the ideal 2θ axis with the following relationship (Scarlett *et al.*, 2011):

$$\sin(\mathit{tth\_new}) = - u(y) * \sin(\mathit{tth\_middle}) / \mathit{Rs},$$

where $\mathit{tth\_new}$ is the new 2θ axis, u is the offset from the sample voxel at the middle of the sample, $\mathit{tth\_middle}$ is the 2θ axis corresponding to the known sample-to-detector distance from the detector calibration and Rs is the sample-to-detector distance.

However, in contrast to laboratory arc diffractometers, Rs is not constant in area detectors and is instead a function of 2θ. This can be easily modelled with high accuracy (i.e. error of several orders of magnitude smaller than the experimental 2θ axis step size) using a 4th degree polynomial. One can then construct a 2D grid where each pixel corresponds to a single 2θ axis. The real space XRD-CT data are passed in this 2θ grid performing a 3D interpolation and the Radon transform of the interpolated XRD-CT volume is calculated. The process is repeated for nA tomographic angles by rotating the 2θ grid accordingly. In TOPAS this was modelled by assigning a unique *th2_offset* to each structure model in the real space images according to the following equation (Rowles & Buckley, 2017):

$$\mathit{th2\_offset} = -57.295779 * u * \mathit{Sin}(2*\mathit{Th}) / (a * \mathit{Xo}^4 + b * \mathit{Xo}^3 + c * \mathit{Xo}^2 + d * \mathit{Xo} + e);$$

Where u is the distance of the specific voxel from the middle of the sample in μm, Th and Xo are the known 2θ axis corresponding to the known sample-to-detector distance from the detector calibration in rad and degrees respectively and a, b, c, d, and e are the calculated coefficients from the 4th degree polynomial.

For the Ni XRD-CT parallax simulation test, the sample-to-detector distance was considered to be 1000 mm and the sample size equal to 24.2 mm (121 voxels × 0.2 mm step size); this is identical to the parameters used for the experimental XRD-CT data presented in the next section. The results from the Rietveld analysis of the Ni simulated XRD-CT data containing parallax artefact are presented in Figure 4. The conventional approach yields accurate results regarding the Ni phase distribution; however, this doesn't mean that all results are accurate, as the Ni lattice parameter and crystallite size maps clearly contain artefacts and the distribution of the respective values are wrong (FBP + Rietveld Rwp = 18.4 %). On the other hand, the DLSR approach yields the same result as before (Figure 3), retaining the correct physico-chemical information (DLSR Rwp = 0.51 % after 25 iterations in 16.4 min).

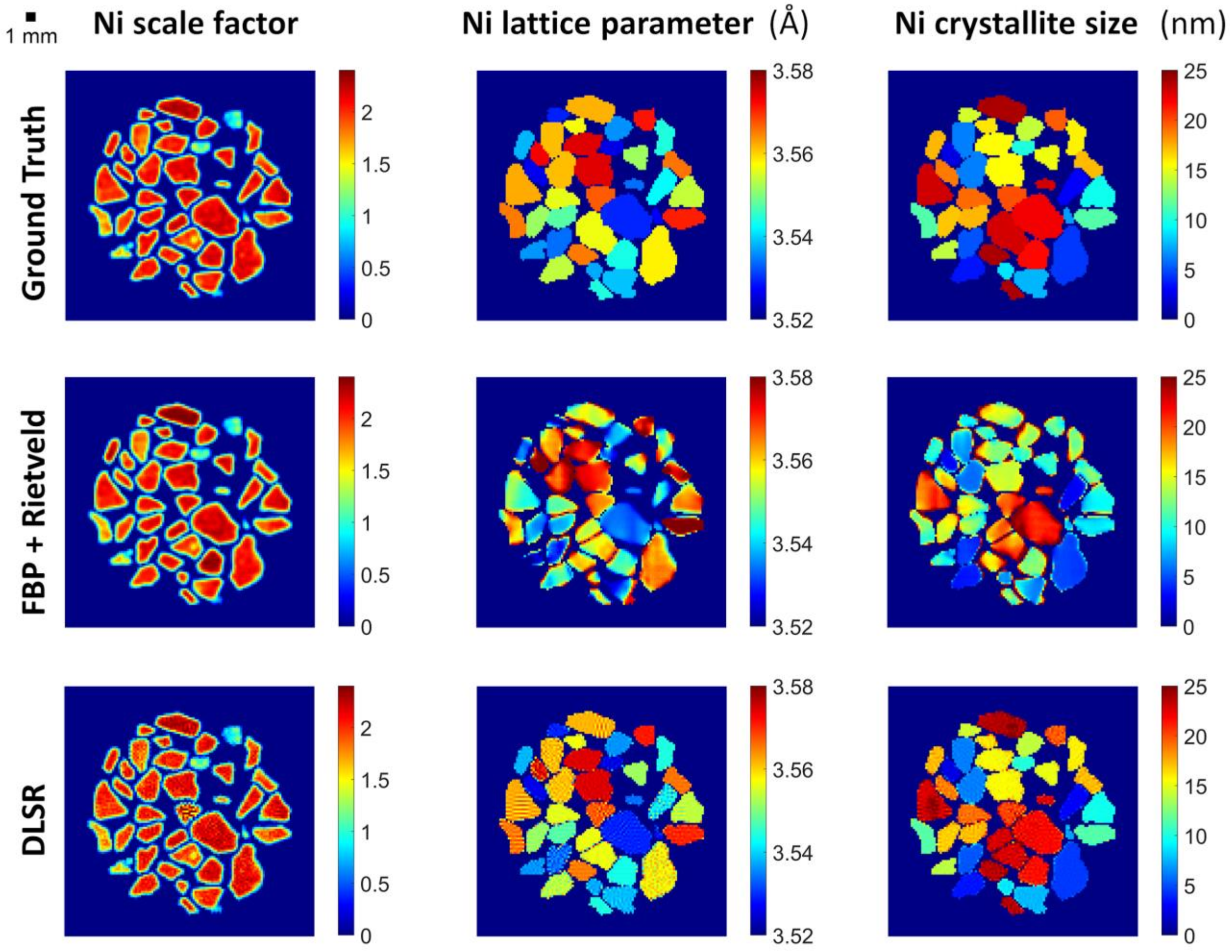

Figure 4: Parallax XRD-CT simulations. Top row: The ground truth images from the simulated Ni XRD-CT data, Middle row: Results obtained from the sequential Rietveld analysis of the reconstructed XRD-CT data containing parallax artefact, Bottom row: Images derived from the Rietveld reconstruction of the XRD-CT data containing parallax artefact using the DLSR approach.

Experimental XRD-CT data

The summed XRD-CT image of the phantom sample is presented in Figure 5a showing the cross section of the four glass pipettes containing the powder samples. Phase identification (Figure S13) verified the presence of TiO_2 rutile (ICSD: 33837 (Kazumasa Sugiyama & Yoshio Takéuchi, 1991)), MgO (ICSD: 9863(SASAKI *et al.*, 1979)) and SiC (ICSD: 603798 (Li & Bradt, 1986)). Figure 5b shows a magnified region of the XRD-CT summed diffraction pattern. It can be seen that the MgO peak is split which is a result of the parallax artefact. As previously discussed, this phase cannot be modeled using a single MgO structure regardless of the tomographic scan range (0-180° or 0-360°). As illustrated in Figure 5b, one has to use at least two copies of the same structure to model the MgO diffraction pattern. For the conventional approach using the FBP reconstruction algorithm and the sequential Rietveld analysis, two MgO structure models were used to model the MgO diffraction peaks in an attempt to overcome the parallax artefact. The peak splitting of the MgO phase and the position of the TiO_2 and SiC phases during the 0-360° scan is shown in section S8. It should be emphasized that the DLSR approach takes into account the parallax artefact and therefore only one MgO structure model is needed. Before proceeding with the diffraction analysis and to simplify the refined model, the signal generated from the glass pipettes was subtracted from the sinogram XRD-CT data (see section S9).

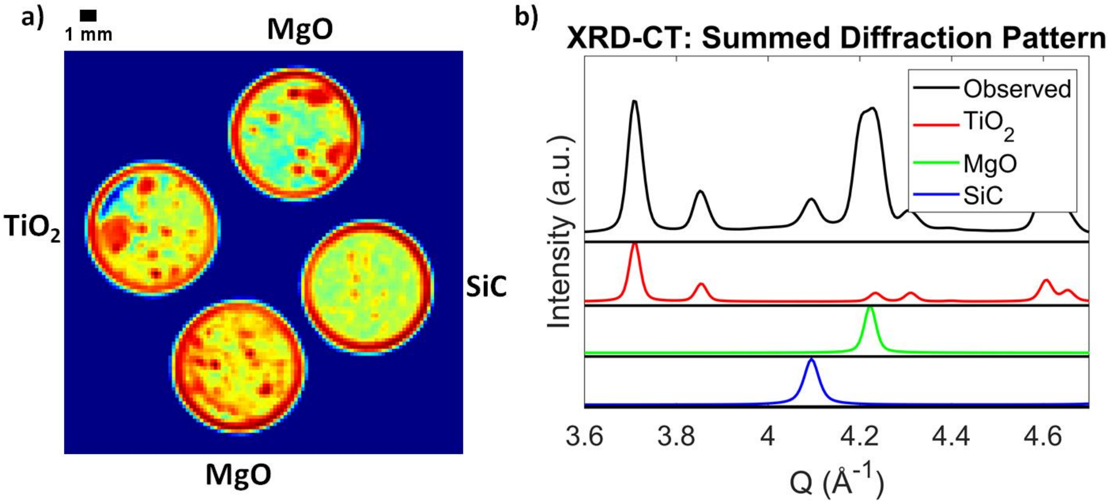

Figure 5: Left: Normalised summed XRD-CT image showing the four samples (TiO_2, SiC and 2× MgO) in their sample holders. Right: Magnified region of the XRD-CT summed diffraction pattern showing the splitting of a MgO diffraction peak.

The 0-360° XRD-CT scan was used to extract projected diffraction patterns (i.e. from the sinogram XRD-CT data) collected at tomographic angles where the samples were at an orientation which minimised the parallax artefact. Specifically, the diffraction patterns were exported from the XRD-CT sinogram data which originated from the edge of the glass pipettes. This results in diffraction patterns that represent well the MgO, TiO_2 and SiC samples as the peak position and broadening artefacts caused by the parallax phenomenon are minimised (i.e. due to correct sample-to-detector distance and minimum sample cross section respectively). The initial peak shape profile was calculated using a CeO2calibrant (ICSD 72155; Wołcyrz & Kepinski, 1992) and then further refined by performing a full-profile analysis of the aforementioned pattern from the phantom sample (see Section S10). The peak shape parameters were shared for the four phases while the individual crystallite size was refined. This led to excellent peak fit results (Figures S17-18) which was then used for both the conventional reconstruction and DLSR approaches. The full profile analysis results are summarized in Table S5 and serve as a means to assess the validity of the corresponding results obtained with the conventional and DLSR approaches.

As discussed previously, the TOPAS implementation of the DLSR approach can handle multi-phase systems with varying crystallographic properties as is the case with the three powder samples used in this work. To optimize the reconstruction process, a mask was applied to decrease the total number of refined parameters and each voxel was assigned a scale factor

(TiO_2, MgO and SiC), lattice parameters (*a* and *c* for TiO_2, *a* for MgO and *a* for SiC), crystallite size (TiO_2, MgO and SiC) and four global pseudo-Voigt peak shape parameters (GU, GV, GW and LX) which on refinement changed insignificantly from the starting model (i.e. less than 1% change). The background in the diffraction patterns was fairly flat after the subtraction of the glass signal; a 2nd degree Chebyshev polynomial was enough to model it. In contrast to the single peak fitting analysis of the Ni simulated XRD-CT, a full diffraction profile analysis was performed requiring computational resources of ca. 95 GB RAM (Rwp = 9.47 % in ca. 150 min for the 0-180° scan and Rwp = 8.65 % in 296 min for the 0-360° scan). The results from the Rietveld analysis of the XRD-CT data are summarized in Table S6.

The TiO_2 rutile phase analysis from the 0-180° and 0-360° scans using both the conventional (i.e. XRD-CT images reconstructed using the FBP algorithm followed by sequential Rietveld analysis) and DLSR approaches are presented in Figure 6. It can be seen that the scale factor maps obtained with the DLSR approach are noisier than the conventional approach for both the 0-180° and 0-360° scans. This is to be expected and is in agreement with the simulation analysis presented previously in Figures 3 and 4. From our experience, the scale factor maps obtained with the conventional approach invariably describe accurate phase distributions. Taking this into account, we have developed TOPAS DLSR scripts where phase dependent scale factor maps, obtained from the conventional approach, are a function of a single refined global parameter. This has the advantage of stabilising the Rietveld refinements.

It can also be seen that for the 0-180° XRD-CT scan, the conventional approach leads to overestimated values for both TiO_2 lattice parameters *a* and *c* (mean value of 4.612 and 2.957 Å respectively). For the 0-360° XRD-CT scan, the conventional approach leads to results very close to the ones obtained with the DLSR method (mean value of 4.593 and 2.956 Å for TiO_2 lattice parameters *a* and *c* respectively). However, this results in larger crystallite size errors for the TiO_2 phase (mean value of 26 nm compared to 53 nm); the 0-360° XRD-CT scan with the conventional approach leads to smaller values (i.e. broader peaks). In contrast, the DLSR approach yields correct peak positions (mean value of 4.593 and 2.956 Å for TiO_2 lattice parameters *a* and *c* respectively) and sharp peaks (mean value of 116 and 134 nm for TiO_2 crystallite sizes for the 0-180° and the 0-360° XRD-CT scans respectively). It should be noted that the scale factor maps obtained with the DLSR approach are less noisy for the 0-180° than the 0-360° XRD-CT scan; both scans comprise the same number of angles and this should be taken into account when designing future XRD-CT experiments with large samples.

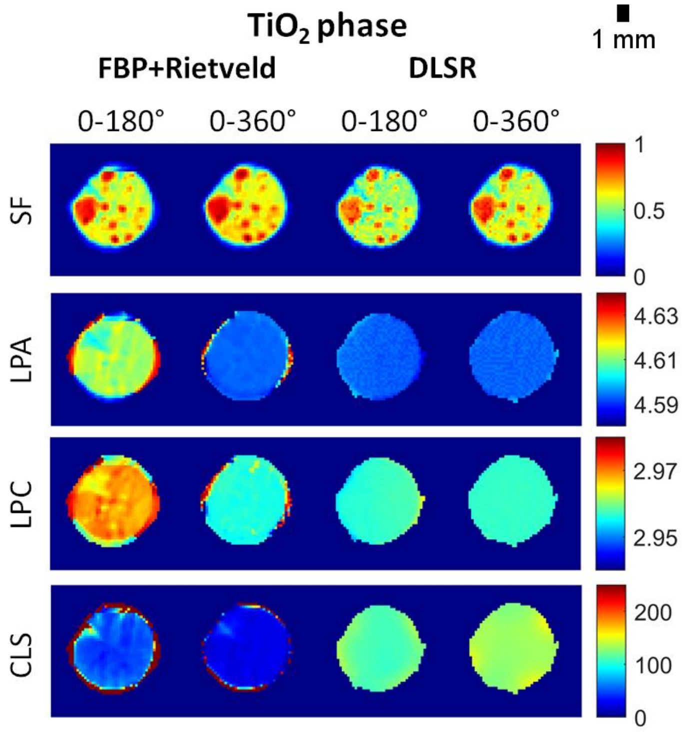

Figure 6: Top row: TiO_2 normalised scale factor (SF) maps, Second row: TiO_2 lattice parameter *a* (LPA) maps (colorbar axis in Å), Third row: TiO_2 lattice parameter *c* (LPC) maps (colorbar axis in Å), Bottom row: TiO_2 crystallite (CLS) maps (colorbar axis in nm).

The results regarding the MgO phase are presented in Figure 7; for the conventional analysis, two MgO cells were used to model the parallax induced peak splitting. FBP reconstructed XRD-CT images, using a single MgO phase, even in the absence of peak splitting, often yield meaningless results. The results from the conventional approach presented in Figure 7 correspond to the mean value obtained using the two MgO structure models (i.e. mean value for scale factor, lattice parameter and crystallite size). Regardless of this correction, it can be seen that the MgO lattice parameter maps contain artefacts for both the 0-180° and 0-360° XRD-CT scans (i.e. non-uniform lattice parameter maps). In contrast, the DLSR approach, requiring a single MgO structure model, leads to uniform maps for the MgO lattice parameter (mean value of 4.212 Å) and crystallite size (mean value of 157 nm and 205 nm for the 0-180° and the 0-360° XRD-CT scans respectively) for both powder samples. Similar to the TiO_2 phase, the values obtained for the MgO crystallite size is significantly different for the two approaches; demonstrating the artificial broadening caused by the parallax artefact.

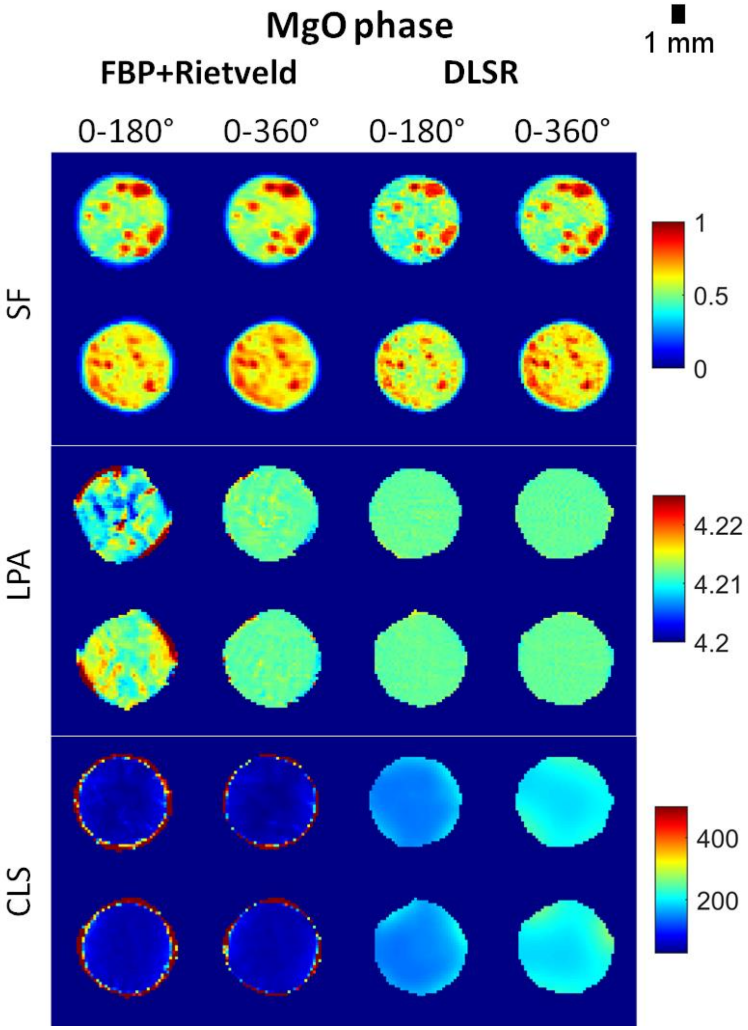

Figure 7: Top two rows: MgO normalised scale factor (SF) maps, Middle two rows: MgO lattice parameter a (LPA) maps (colorbar axis in Å), Bottom two rows: MgO crystallite (CLS) maps (colorbar axis in nm).

Finally, the results regarding the SiC phase are presented in Figure 8. Here, it is seen that for the 0-180° XRD-CT scan, in contrast to the TiO_2 results, the conventional approach leads to underestimated values for the SiC lattice parameter (mean value of 4.344 Å). The error for the crystallite size values is lower; this can be attributed to the broader peaks compared to the TiO_2 and MgO phases. It should be noted that the conventional approach for the 0-360° XRD-CT scan leads to higher errors and lower values for the crystallite size (mean value of 27 nm and 18 nm for the 0-180° and the 0-360° XRD-CT scans respectively). In contrast, the DLSR approach yields correct and uniform results for the SiC lattice parameter (mean value of 4.358 Å for both 0-180° and 0-360° scans) and crystallite size (mean value of ca. 40 nm for both scans) regardless of the angular range covered during the tomographic scan.

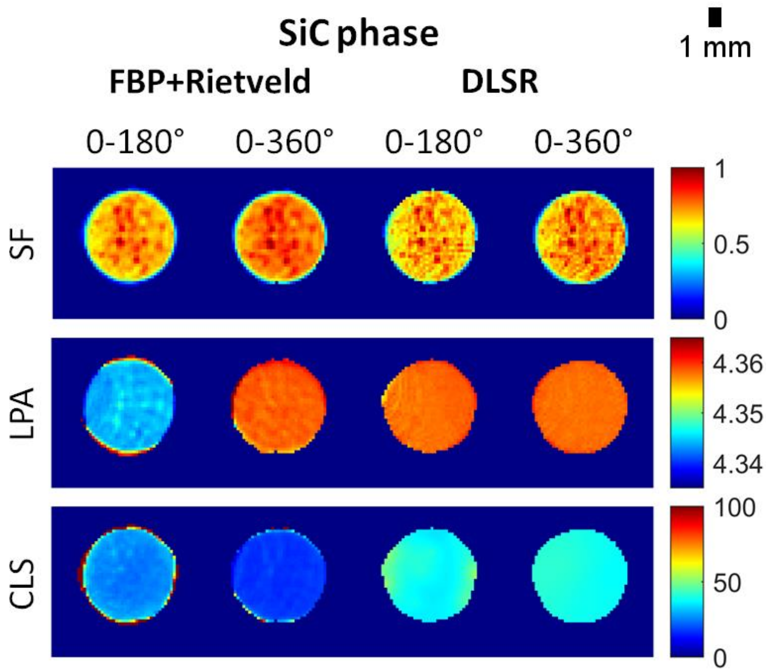

Figure 8: Top row: SiC normalised scale factor (SF) maps, Middle row: SiC lattice parameter a (LPA) maps (colorbar axis in Å), Bottom row: SiC crystallite (CLS) maps (colorbar axis in nm).

Summary & Conclusions

We have developed a new tomographic reconstruction algorithm which solves the parallax artefact problem in XRD-CT. The solution is of consequence for large samples where X-rays, scattered along the sample, arrive at a multitude of detector elements. This phenomenon leads to loss of physico-chemical information (i.e. information regarding peak position and shape) that cannot be retrieved with conventional reconstruction approaches. We have demonstrated that our approach works with both simulated and experimental XRD-CT data. It is expected that it will open a new path for X-ray scattering-based CT techniques and their application to samples that are several cm in diameter. Overcoming the parallax barrier is especially important for functional materials and devices, such as catalytic reactors, batteries and fuel cells where the chemistry in idealised cells can vary significantly from their industrial-size counterparts (e.g. different degradation mechanisms taking place at different length scales).

Our approach is not limited to XRD-CT and can be applied to all chemical tomography techniques. For example, the DLSR method can prove invaluable to the future implementation of neutron powder diffraction computed tomography of very large samples. However, the drawback of the developed approach is that it is computationally expensive. There are options one can explore to speed up the reconstruction process, like using binary files which can increase the reading time (expected 4x fold increase in speed) or use faster CPUs. Regarding the memory requirements, one can perform an iterative reconstruction when one ray or one projection is being processed at a time rather than all diffraction patterns present in the XRD-CT sinogram data. This will however increase significantly the time to converge to a useful solution. The stability of the reconstruction can also be significantly improved by using the FBP solution for the scale factors and refining other properties such as lattice parameters and crystallite sizes. Finally, it should be pointed out that future implementations of the current solution could go beyond least-squares minimisation such as machine learning approaches which could overcome the current limitations of the DLSR method.

Author contributions

A.V. and S.D.M.J. conceived the DLSR algorithm. A.V. and A.A.C. implemented the DLSR approach on the TOPAS Academic v7 with contributions from D.M., H.D and S.D.M.J. A.V., I.M. and J.D. discussed the parallax artefacts in XRD-CT data collected using an industrial sized PEM fuel cell which inspired this work. The parallax experiment was conceived by A.V. with contributions from D.M., Y.O., S.W.T.P. and S.D.M.J. The 3D printed sample holder was designed by Y.O. The XRD-CT measurements were performed by A.V., Y.O., S.W.T.P and S.D.M.J. O.G., A.C.D. and M.Z. were responsible for P07 instrumentation and setup at the PETRA III, DESY. The XRD-CT data were analysed by A.V. with contributions from D.M., H.D, K.B. and S.D.M.J. A.V. is responsible for writing the manuscript with feedback given by all contributors. A.M.B. directed the research.

Acknowledgements

The authors would like to thank Dr Marco di Michiel for initial discussions on the parallax problem and for motivation to work on this challenging problem. Finden acknowledges funding through the Innovate UK Analysis for Innovators (A4i) program (Project No: 106003). The authors would like to thank Dr Wilm Jones for assistance with the sample preparation and the UK Catalysis Hub for providing the powder samples used in the XRD-CT experiments. We acknowledge DESY (Hamburg, Germany), a member of the Helmholtz Association HGF, for the provision of experimental facilities. Parts of this research were carried out at PETRA III. A.M.B. acknowledges EPSRC (grants EP/R026815/1 and EP/S016481/1)

Data Availability

Copies of simulated and experimental (i.e. sinogram volume after centering, cropping and subtracting the background air signal and the glass signal) XRD-CT data can be found at https://doi.org/10.5281/zenodo.4059827. All data are available from the corresponding authors on reasonable request.

References

Álvarez-Murga, M., Bleuet, P., Marques, L., Lepoittevin, C., Boudet, N., Gabarino, G., Mezouar, M. & Hodeau, J.-L. (2011). *J. Appl. Crystallogr.* **44**, 163–171.

Anders P. Kaestner, Beat Munch & Pavel Trtik (2011). *Opt. Eng.* **50**, 1–10.

Artioli, G., Cerulli, T., Cruciani, G., Dalconi, M. C., Ferrari, G., Parisatto, M., Rack, A. &

Tucoulou, R. (2010). *Anal. Bioanal. Chem.* **397**, 2131–2136.

Basile, F., Benito, P., Bugani, S., De Nolf, W., Fornasari, G., Janssens, K., Morselli, L., Scavetta, E., Tonelli, D. & Vaccari, A. (2010). *Adv. Funct. Mater.* **20**, 4117–4126.

Beale, A. M., Gibson, E. K., O'Brien, M. G., Jacques, S. D. M., Cernik, R. J., Michiel, M. D., Cobden, P. D., Pirgon-Galin, Ö., van de Water, L., Watson, M. J. & Weckhuysen, B. M. (2014). *J. Catal.* **314**, 94–100.

Beale, A. M., Jacques, S. D. M., Di Michiel, M., Mosselmans, F. W., Price, S. W. T., Senecal, P., Vamvakeros, A. & Paterson, J. (2018). *Philos. Trans. R. Soc. Math. Phys. Eng. Sci.* **376**, 2110, 20170057.

Beale, A. M., Jacques, S. D. M., Gibson, E. K. & Di Michiel, M. (2014). *Coord. Chem. Rev.* **277–278**, 208–223.

Beister, M., Kolditz, D. & Kalender, W. A. (2012). *Phys. Med.* **28**, 94–108.

Bleuet, P., Welcomme, E., Dooryhée, E., Susini, J., Hodeau, J.-L. & Walter, P. (2008). *Nat. Mater.* **7**, 468–472.

Bonnin, A., Wright, J. P., Tucoulou, R. & Palancher, H. (2014). *Appl. Phys. Lett.* **105**, 084103.

Cedola, A., Campi, G., Pelliccia, D., Bukreeva, I., Fratini, M., Burghammer, M., Rigon, L., Arfelli, F., Chen, R. C., Dreossi, D., Sodini, N., Mohammadi, S., Tromba, G., Cancedda, R. & Mastrogiacomo, M. (2013). *Phys. Med. Biol.* **59**, 189–201.

Claret, F., Grangeon, S., Loschetter, A., Tournassat, C., De Nolf, W., Harker, N., Boulahya, F., Gaboreau, S., Linard, Y., Bourbon, X., Fernandez-Martinez, A. & Wright, J. (2018). *IUCrJ*. **5**, 150–157.

Coelho, A. (2018). *J. Appl. Crystallogr.* **51**, 210–218.

Daemi, S. R., Tan, C., Vamvakeros, A., Heenan, T. M. M., Finegan, D. P., Di Michiel, M., Beale, A. M., Cookson, J., Petrucco, E., Weaving, J. S., Jacques, S., Jervis, R., Brett, D. J. L. & Shearing, P. R. (2020). *Phys Chem Chem Phys*, **22**, 32, 17814-17823.

De Nolf, W. & Janssens, K. (2010). *Surf. Interface Anal.* **42**, 411–418.

Egan, C. K., Jacques, S. D. M., Di Michiel, M., Cai, B., Zandbergen, M. W., Lee, P. D., Beale, A. M. & Cernik, R. J. (2013). *Acta Biomater.* **9**, 8337–8345.

Finegan, D. P., Vamvakeros, A., Cao, L., Tan, C., Heenan, T. M. M., Daemi, S. R., Jacques, S. D. M., Beale, A. M., Di Michiel, M., Smith, K., Brett, D. J. L., Shearing, P. R. & Ban, C. (2019). *Nano Lett.* **19**, 6, 3811-3820.

Finegan, D. P., Vamvakeros, A., Tan, C., Heenan, T. M. M., Daemi, S. R., Seitzman, N., Di Michiel, M., Jacques, S., Beale, A. M., Brett, D. J. L., Shearing, P. R. & Smith, K. (2020). *Nat. Commun.* **11**, 631.

Frølich, S. & Birkedal, H. (2015). *J. Appl. Crystallogr.* **48**, 2019–2025.

Gambino, M., Veselý, M., Filez, M., Oord, R., Ferreira Sanchez, D., Grolimund, D., Nesterenko, N., Minoux, D., Maquet, M., Meirer, F. & Weckhuysen, B. M. (2020). *Angew. Chem. Int. Ed.* **59**, 3922–3927.

Gonzalez, V., Van Loon, A., Price, S., Noble, P. & Keune, K. (2020). *J Anal Spectrom*. **35**, 10, 2267-2273.

Grande, C. A., Blom, R., Middelkoop, V., Matras, D., Vamvakeros, A., Jacques, S. D. M., Beale, A. M., Di Michiel, M., Anne Andreassen, K. & Bouzga, A. M. (2020). *Chem. Eng. J.* **402**, 126166.

Gürsoy, D., Biçer, T., Almer, J. D., Kettimuthu, R., Stock, S. R. & De Carlo, F. (2015). *Philos. Transact. A Math. Phys. Eng. Sci.* **373**, 20140392.

Hansen, P. C. & Jørgensen, J. S. (2018). *Numer. Algorithms*. **79**, 107–137.

Harding, G., Kosanetzky, J. & Neitzel, U. (1987). *Med. Phys.* **14**, 515–525.

Heenan, T., Vamvakeros, A., Tan, C., Finegan, D. P., Daemi, S., Jacques, S. D. M., Beale, A. M., di Michiel, M., Brett, D. J. L. & Shearing, P. R. (2020). *Crystals*. The Detection of Monoclinic Zirconia and Non-Uniform 3D Crystallographic Strain in a Re-Oxidized Ni-YSZ Solid Oxide Fuel Cell Anode

Ihli, J., Jacob, R. R., Holler, M., Guizar-Sicairos, M., Diaz, A., da Silva, J. C., Ferreira Sanchez, D., Krumeich, F., Grolimund, D., Taddei, M., Cheng, W.-C., Shu, Y., Menzel, A. & van Bokhoven, J. A. (2017). *Nat. Commun.* **8**, 809.

Jacques, S. D. M., Di Michiel, M., Beale, A. M., Sochi, T., O'Brien, M. G., Espinosa-Alonso, L., Weckhuysen, B. M. & Barnes, P. (2011). *Angew. Chem. Int. Ed.* **50**, 10148–10152.

Jacques, S. D. M., Di Michiel, M., Kimber, S. A. J., Yang, X., Cernik, R. J., Beale, A. M. & Billinge, S. J. L. (2013). *Nat. Commun.* **4**, 2536.

Jensen, K. M. O., Yang, X., Laveda, J. V., Zeier, W. G., See, K. A., Di Michiel, M., Melot, B. C., Corr, S. A. & Billinge, S. J. L. (2015). *J. Electrochem. Soc.* **162**, A1310–A1314.

Kazumasa Sugiyama & Yoshio Takéuchi (1991). *Z. Für Krist. - Cryst. Mater.* **194**, 305–313.

Kleuker, U., Suortti, P., Weyrich, W. & Spanne, P. (1998). *Phys. Med. Biol.* **43**, 2911–2923.

Leemreize, H., Almer, J. D., Stock, S. R. & Birkedal, H. (2013). *J. R. Soc. Interface*. **10**, 20130319–20130319.

Li, T., Heenan, T. M. M., Rabuni, M. F., Wang, B., Farandos, N. M., Kelsall, G. H., Matras, D., Tan, C., Lu, X., Jacques, S. D. M., Brett, D. J. L., Shearing, P. R., Di Michiel, M., Beale, A. M., Vamvakeros, A. & Li, K. (2019). *Nat. Commun.* **10**, 1497.

Li, Z. & Bradt, R. C. (1986). *J. Mater. Sci.* **21**, 4366–4368.

Liu, H., Kazemiabnavi, S., Grenier, A., Vaughan, G., Di Michiel, M., Polzin, B. J., Thornton, K., Chapman, K. W. & Chupas, P. J. (2019). *ACS Appl. Mater. Interfaces*. **11**, 18386–18394.

Marlton, F., Ivashko, O., Zimmerman, M. v., Gutowski, O., Dippel, A.-C. & Jorgensen, M. R. V. (2019). *J. Appl. Crystallogr.* **52**, 1072–1076.

Martens, I., Vamvakeros, A., Chattot, R., Blanco, M. V., Rasola, M., Pusa, J., Jacques, S. D. M., Bizzotto, D., Wilkinson, D. P., Ruffmann, B., Heidemann, S., Honkimäki, V. & Drnec, J. (2019). *J. Power Sources*, **437**, 226906.

Martens, I., Vamvakeros, A., Martinez, N., Chattot, R., Pusa, J., Blanco, M. V., Fisher, E. A., Asset, T., Escribano, S., Micoud, F., Starr, T., Coelho, A., Honkimäki, V., Bizzotto, D., Wilkinson, D. P., Jacques, S. D. M., Maillard, F., Dubau, L., Lyonnard, S., Morin, A. & Drnec, J. (2020). Holistic Multi-scale Imaging of Oxygen Reduction Reaction Catalyst Degradation in Operational Fuel Cells.

Matras, D., Jacques, S. D. M., Godini, H. R., Khadivi, M., Drnec, J., Poulain, A., Cernik, R. J. & Beale, A. M. (2018). *J. Phys. Chem. C*. **122**, 2221–2230.

Matras, D., Jacques, S. D. M., Poulston, S., Grosjean, N., Estruch Bosch, C., Rollins, B., Wright, J., Di Michiel, M., Vamvakeros, A., Cernik, R. J. & Beale, A. M. (2019). *J. Phys. Chem. C*. **123**, 1751–1760.

Matras, D., Vamvakeros, A., Jacques, S. D. M., Middelkoop, V., Vaughan, G., Agote Aran, M., Cernik, R. J. & Beale, A. M. (2020). *Phys Chem Chem Phys*, **22**, 18964-18975.

Matras, D., Vamvakeros, A., Jacques, S., Grosjean, N., Rollins, B., Poulston, S., Stenning, G. B. G., Godini, H., Drnec, J., Cernik, R. J. & Beale, A. M. (2020). *Faraday Discuss.*

Middelkoop, V., Vamvakeros, A., de Wit, D., Jacques, S. D. M., Danaci, S., Jacquot, C., de Vos, Y., Matras, D., Price, S. W. T. & Beale, A. M. (2019). *J. CO2 Util.* **33**, 478–487.

O'Brien, M. G., Jacques, S. D. M., Di Michiel, M., Barnes, P., Weckhuysen, B. M. & Beale, A. M. (2012). *Chem. Sci.* **3**, 509–523.

Palancher, H., Tucoulou, R., Bleuet, P., Bonnin, A., Welcomme, E. & Cloetens, P. (2011). *J. Appl. Crystallogr.* **44**, 1111–1119.

Price, S. W. T., Geraki, K., Ignatyev, K., Witte, P. T., Beale, A. M. & Mosselmans, J. F. W. (2015). *Angew. Chem.* **127**, 10024–10027.

Price, S. W. T., Ignatyev, K., Geraki, K., Basham, M., Filik, J., Vo, N. T., Witte, P. T., Beale, A. M. & Mosselmans, J. F. W. (2015). *Phys. Chem. Chem. Phys.* **17**, 521–529.

Price, S. W. T., Martin, D. J., Parsons, A. D., S\lawiński, W. A., Vamvakeros, A., Keylock, S. J., Beale, A. M. & Mosselmans, J. F. W. (2017). *Sci. Adv.* **3**, e1602838.

Price, S. W. T., Van Loon, A., Keune, K., Parsons, A. D., Murray, C., Beale, A. M. & Mosselmans, J. F. W. (2019). *Chem. Commun.* **55**, 1931–1934.

Rowles, M. R. & Buckley, C. E. (2017). *J. Appl. Crystallogr.* **50**, 240–251.

Ruiz-Martínez, J., Beale, A. M., Deka, U., O'Brien, M. G., Quinn, P. D., Mosselmans, J. F. W. & Weckhuysen, B. M. (2013). *Angew. Chem. Int. Ed.* **52**, 5983–5987.

Sanchez, D. F., Grolimund, D., Hubert, M., Bleuet, P. & Laurencin, J. (2017). *Int. J. Hydrog. Energy*. **42**, 1203–1211.

SASAKI, S., FUJINO, K. & TAKÉUCHI, Y. (1979). *Proc. Jpn. Acad. Ser. B*. **55**, 43–48.

Scarlett, N. V. Y., Rowles, M. R., Wallwork, K. S. & Madsen, I. C. (2011). *J. Appl. Crystallogr.* **44**, 60–64.

Senecal, P., Jacques, S. D. M., Di Michiel, M., Kimber, S. A. J., Vamvakeros, A., Odarchenko, Y., Lezcano-Gonzalez, I., Paterson, J., Ferguson, E. & Beale, A. M. (2017). *ACS Catal.* **7**, 2284-2293.

Sheppard, T. L., Price, S. W. T., Benzi, F., Baier, S., Klumpp, M., Dittmeyer, R., Schwieger, W. & Grunwaldt, J.-D. (2017). *J. Am. Chem. Soc.* **139**, 7855–7863.

Sottmann, J., Di Michiel, M., Fjellvåg, H., Malavasi, L., Margadonna, S., Vajeeston, P., Vaughan, G. B. M. & Wragg, D. S. (2017). *Angew. Chem. Int. Ed.* **56**, 11385–11389.

Stock, S. R. & Almer, J. D. (2012). *J. Appl. Crystallogr.* **45**, 1077–1083.

Stock, S. R., De Carlo, F. & Almer, J. D. (2008). *J. Struct. Biol.* **161**, 144–150.

Stock, S. R., Laugesen, M., Birkedal, H., Jakus, A., Shah, R., Park, J.-S. & Almer, J. D. (2019). *J. Appl. Crystallogr.* **52**, 40–46.

Tonin, G., Vaughan, G. B. M., Bouchet, R., Alloin, F., Di Michiel, M. & Barchasz, C. (2020). *J. Power Sources*. **468**, 228287.

Valentini, L., Artioli, G., Voltolini, M. & Dalconi, M. C. (2012). *J. Am. Ceram. Soc.* **95**, 2647–2652.

Valentini, L., Dalconi, M. C., Parisatto, M., Cruciani, G. & Artioli, G. (2011). *J. Appl. Crystallogr.* **44**, 272–280.

Vamvakeros, A., Jacques, S. D. M., Di Michiel, M., Matras, D., Middelkoop, V., Ismagilov, I. Z., Matus, E. V., Kuznetsov, V. V., Drnec, J., Senecal, P. & Beale, A. M. (2018). *Nat. Commun.* **9**, 4751.

Vamvakeros, A., Jacques, S. D. M., Di Michiel, M., Middelkoop, V., Egan, C. K., Cernik, R. J. & Beale, A. M. (2015). *J. Appl. Crystallogr.* **48**, 1943–1955.

Vamvakeros, A., Jacques, S. D. M., Di Michiel, M., Senecal, P., Middelkoop, V., Cernik, R. J. & Beale, A. M. (2016). *J. Appl. Crystallogr.* **49**,.

Vamvakeros, A., Jacques, S. D. M., Middelkoop, V., Di Michiel, M., Egan, C. K., Ismagilov, I. Z., Vaughan, G. B. M., Gallucci, F., Van Sint Annaland, M., Shearing, P. R., Cernik, R. J. & Beale, A. M. (2015). *Chem. Commun.* **51**, 12752–12755.

Vamvakeros, A., Matras, D., Jacques, S. D. M., di Michiel, M., Middelkoop, V., Cong, P., Price, S. W. T., Bull, C. L., Senecal, P. & Beale, A. M. (2020). *Catal. Today*.

Vamvakeros, A., Matras, D., Jacques, S. D. M., di Michiel, M., Price, S. W. T., Senecal, P., Aran, M. A., Middelkoop, V., Stenning, G. B. G., Mosselmans, J. F. W., Ismagilov, I. Z. & Beale, A. M. (2020). *J. Catal.* **386**, 39–52.

Vanmeert, F., Van der Snickt, G. & Janssens, K. (2015). *Angew. Chem. Int. Ed.* **54**, 3607–3610.

Voltolini, M., Dalconi, M. C., Artioli, G., Parisatto, M., Valentini, L., Russo, V., Bonnin, A. & Tucoulou, R. (2013). *J. Appl. Crystallogr.* **46**, 142–152.

Wittig, N. K., Palle, J., Østergaard, M., Frølich, S., Birkbak, M. E., Spiers, K. M., Garrevoet, J. & Birkedal, H. (2019). *ACS Nano*. **13**, 12949–12956.

WoŁcyrz, M. & Kepinski, L. (1992). *J. Solid State Chem.* **99**, 409–413.

Wragg, D. S., O'Brien, M. G., Di Michiel, M. & Lonstad-Bleken, F. (2015). *J. Appl. Crystallogr.* **48**, 1719–1728.

(1953). Standard X-ray diffraction powder patterns National Bureau of Standards Circular (U.

S.).